Modeling of gas–liquid reactions in porous membrane microreactors

Jigar M. Jani, H. Can Aran, Matthias Wessling, Rob G.H. Lammertink*

Soft Matter, Fluidics and Interfaces, MESA+ Institute for Nanotechnology, P.O. Box 217, 7500 AE Enschede, The Netherlands

ABSTRACT

This work provides a numerical model studying mass transport and heterogeneously catalyzed reactions in a porous membrane microreactor. The hydrogenation of nitrite over a Pd catalyst was used as a model reaction. The influence of liquid flow rates, initial nitrite concentration and catalytic membrane layer thickness (wetting thickness) on the conversion was studied. Firstly, a kinetic model was implemented based on the correlations available for reaction kinetics from literature. The results were validated using experimental results and it was found that the process is best described by Langmuir–Hinshelwood reaction kinetics. Secondly, to obtain an optimized reactor geometry, boundary conditions were derived, which represent the reactant concentration at the microreactor inner wall as a function of catalytic layer properties. An optimum in conversion was found for varying catalytic membrane layer thickness. The initial increase in conversion with increasing catalytic layer thickness is due to enhanced catalyst area. The conversion later reduces due to gaseous reactant mass transfer limitation, for even thicker layers. This study provides detailed understanding of the mass transfer taking place in membrane microreactors. It also provides routes towards optimized reactor configurations, which allows for more efficient catalyzed gas–liquid reaction processes.

1. Introduction

Membrane based operations including separations, reactions and contacting have received significant attention in the last few decades. They offer advantages, such as ease of operation and scale-up, low operational cost, high selectivity and affordable energy requirements. Membrane reactors for gas–liquid processes are exploited to achieve stable gas–liquid interfaces [1,2]. Recently, porous hydrophobic membrane microreactors were employed for effective gas–liquid contacting [3]. Catalytic membrane microreactors are useful for multiphase reaction systems involving gas–liquid–solid (G–L–S) [4]. This design provides a way to achieve less emission, controlled chemistry and enhanced efficiency [5–12]. Membrane reactors also help to reduce diffusional resistance to mass transfer, giving higher catalytic activities compared to traditional three-phase reactors, e.g., slurry reactors [13–17], packed bed and trickle-bed reactors [18–23]. An experimental study confirmed that these improvements are mainly due to the intense multiphase contacting [24]. Several reactions have been investigated including the removal of nitrite and nitrate ions from ground water [25–29]. Such membrane reactors exploit mainly three functions: (i) facilitate contact between gas and liquid phases; (ii) provide support to immobilize the catalyst; and

(iii) separate inlet conditions for the reactants, providing flexibility regarding gas and liquid flow rates.

Hollow fiber membrane reactors provide a suitable configuration for heterogeneous catalyzed processes. The reactants are separated from each other by a porous hollow fiber membrane. The resulting catalytic reaction zone is usually $8-70\,\mu m$ thick [30]. Liquid reactants come into direct contact with the gaseous reactants in the catalytic regions of the membrane reactors [29,30].

Gas–liquid contacting and catalytic reactions in membrane contactors and reactors have been modeled before [31–35]. Cini and Harold showed experimentally that tubular ceramic membranes can be utilized to achieve multiphase heterogeneous catalytic reactions [31]. The gas containing volatile reactants flowing in tubular core comes in contact with liquid containing non-volatile dissolved constituents flowing in the shell side of the reactor at the catalytically impregnated γ-Al_2O_3 layer. They observed an increase in reaction rate of up to a factor of 20 for tubular membrane supported catalyst compared to fully wetted pellets. Wang et al. developed a theoretical model to understand the gas–liquid contacting under two operating conditions of fully wetted and non-wetted mode in microporous hollow fiber membranes [32]. Their simulation results showed that gas (CO_2) absorption in the non-wetted mode of operation is six times higher than those in the wetted mode of operation. They reported a 20% reduction in overall mass transfer for 5% wetted membrane pores. Kumar et al. studied the catalytic reactions on both sides

* Corresponding author. Tel.: +31 53 489 2063; fax: +31 53 489 2882.
E-mail address: r.g.h.lammertink@utwente.nl (R.G.H. Lammertink).

(tube and shell side) of tubular membrane reactors [33]. They implemented a model to study different catalysts and catalytic dehydrogenation of ethylbenzene to produce styrene in a tubular membrane reactor. Tsai et al. performed two-dimensional simulations to study partial oxidation of methane to syngas in three-layered catalytic membrane reactor. They compared the results with conventional fixed-bed reactor and found that membrane reactors can be used to mitigate severe temperature rise in exothermic reactions [34]. Nagy developed a mathematical model that predicts mass transfer rates and the concentration distribution as a function of the physiochemical parameters, that involves diffusive and convective flow through the catalytic membrane layer [35]. Li and Tan [36] developed theoretical models for membrane reactors to describe mass transfer and chemical reactions taking place either in the hollow fiber lumen or in the shell side. Their results suggested axial dispersion plays a crucial role for the reactions taking place in the shell-side for $Pe > 40$. They also showed that reaction kinetic parameters can be obtained once the reaction mechanism is confirmed.

Gervais et al. have performed a detailed study to identify the parameters that affect the mass transfer and surface reactions in microfluidic devices [37]. Using analytical and modeling approaches, they characterized the transport mechanism towards the stationary surfaces in the absence of a boundary layer and proposed methods to obtain the diffusion/reaction mass transfer coefficient. These mass transfer coefficients can be used to obtain bulk and surface concentrations along the device. The formation of moving concentration fronts in long channels was also analyzed and its propagation velocity was correlated with experimental parameters [37]. The interplay between the flow and interfacial mass transfer is an important factor for systems involving reactive boundaries [38]. There have been several attempts using two-dimensional (2D) models, where both axial and radial concentration profiles of the reactants are obtained [39–43]. There are multiple ways to perform such 2D simulations such as finite difference [44], finite element [45] or orthogonal collocations.

In this work, 2D CFD simulations are performed to study the effects of reaction parameters (i.e. initial reactant concentrations, flow rates, reaction rate constant) and geometrical parameters (i.e., porosity, tortuosity and wetted catalytic layer thickness) on the microreactor performance. An analytical boundary condition is developed representing the concentration profiles for liquid and gaseous reactants along the axial position of the inner wall of the microreactor.

From the design perspective, the numerical simulations and mathematical model developed here represent an important tool for analyzing gas and liquid transport/reaction in a porous membrane microreactor. It allows to:

- Predict diffusive and convective mass transfer phenomena for catalytic chemical reactions in membrane microreactors.
- Evaluate gas and liquid concentration profiles along the axial length of the membrane microreactor.
- Analyze the correct description of the reaction rate expression.
- Design a porous membrane microreactor to maximize the conversion.

2. Modeling of reaction kinetics

In order to describe the mass transfer, the reaction rate expression has to be defined accurately. The schematic representation of the microreactor concept is presented in Fig. 1. The liquid phase, containing one of the reactants, flows through the lumen side of the porous reactor. Gaseous reactants diffuse from the shell side to meet the liquid at the catalyst surface in the wetted γ-Al_2O_3 layer where the reaction takes place.
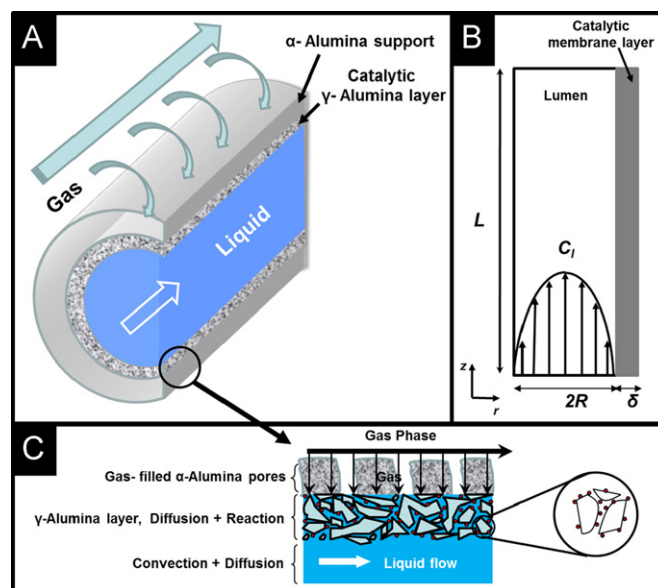

Fig. 1. (A) Schematic representation of a gas–liquid–solid reaction in a hollow fiber membrane microreactor. (B) Two-dimensional representation of computational domain of hollow fiber membrane microreactor. (C) Illustration of tubular membrane reactor.

The concept of the reactor has been successfully implemented for the hydrogenation of nitrites in water [29]. The hydrogenation of nitrite ions (NO_2^-) over palladium (Pd) catalyst in aqueous phase is described as [24–27,46,47]

$$2NO_2^- + 3H_2 \xrightarrow{Pd} N_2 + 2OH^- + 2H_2O \tag{1}$$
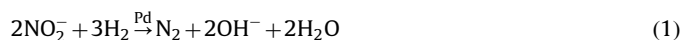
Ideally, nitrites are converted to nitrogen at ambient reaction conditions. The experimental investigation on the kinetics of the hydrogenation of nitrites was recently performed [28,26]. A detailed kinetic study involving catalyst activity and selectivity measurements, over wide range of reactant concentrations and operating conditions, was also performed [25]. They found that the hydrogenation of nitrite follows Langmuir–Hinshelwood (LH) reaction kinetics. Aran et al. showed that when H_2 was pre-dissolved in the aqueous nitrite stream, the reaction was kinetically limited by the H_2 concentration. However, when H_2 was fed through the porous hydrophobic membrane support, the hydrogenation of nitrite was independent of the hydrogen concentration over a wide range [29]. Even when the equilibrium H_2 concentration was below the nitrite concentration, the effective gas–liquid contacting resulted in a zeroth-order reaction rate expression in H_2. Thus, for the LH reaction rate expression, the nitrite disappearance rate is assumed to be independent of hydrogen concentration in this study, giving the following expression:

$$R_{LH} = k_{LH} \frac{K_{ads}C_l}{1 + K_{ads}C_l} \tag{2}$$

where R_{LH} is the LH reaction rate, K_{ads} is the adsorption coefficient, k_{LH} is the LH reaction rate constant, and C_l is the nitrite concentration.

The experimental results of the catalytic reduction of nitrite over Pd catalyst were obtained in terms of conversion and selectivity over a wide range of initial reactant concentrations [26,48]. Several experimental works [48,26] have reported the following kinetic rate expression:

$$R_s = k_s \cdot C_l^n \cdot C_g^m \tag{3}$$

where R_s is the power-law reaction rate, k_s is the reaction rate constant, n is the nitrite reaction order and m is the hydrogen

reaction order. Chinthaginjala et al. [26] have reported the reaction order for nitrite (n) to be around 0.7 in their work. This suggests that the surface coverage of nitrite is relatively low. Matatov-Meyal et al. [48] have reported the reaction order to vary from 0 to 1 for nitrite and hydrogen. This corresponds to zero-order (saturated system) and first-order (diluted system) adsorption on the catalyst surface. Normally, the initial reactant concentration is at millimolar scale, and the kinetic rate expression can be simplified to a first-order equation for nitrite. The equilibrium solubility of H_2 in aqueous nitrite solution is considered to be 0.78 mmol/l at 25 °C.

To gain accurate kinetic parameters for Eqs. (2) and (3), numerical simulations are performed and validated with experimental results. All the governing equations described in Section 3 are solved simultaneously and the results are discussed in Section 4.

3. A catalytic membrane microreactor model

This section comprises the mass balance equations for transport through the lumen of hollow fiber with an immobilized catalytic layer. A schematic representation of the membrane microreactor is shown in Fig. 1a and b. The reactants enter through the fiber lumen under laminar conditions and then diffuse into the catalytic porous γ-Al_2O_3 layer. The pores of the α-Al_2O_3 support are filled with gas and the γ-Al_2O_3 layer is wetted with liquid (Fig. 1c). The catalytic reaction takes place on the surface of immobilized catalyst in the γ-Al_2O_3 layer. A radial concentration gradient will build up in the liquid phase, which should be balanced by the diffusive flux at the inner wall of the hollow fiber.

The model under steady-state and isothermal conditions is described using the following assumptions:

- Parabolic velocity profile in the fiber lumen.
- Porous support exhibits no catalytic activity.
- Uniform pore size distribution.
- Support is fully gas filled (α-Al_2O_3), catalytic layer is liquid filled (γ-Al_2O_3).

The steady-state mass balance in cylindrical co-ordinates for the hollow fiber membrane microreactor can be written as follows:

$$u_z \frac{\partial C_l}{\partial z} = D_l \left(\frac{\partial^2 C_l}{\partial r^2} + \frac{1}{r} \frac{\partial C_l}{\partial r} \right) \quad (0 < r < R) \tag{4}$$

where z is the axial position (m), u_z is the axial liquid velocity (m/s), D_l is the diffusion coefficient for reactants in the liquid (m^2/s), r is the radial position (m). The parabolic velocity profile in the liquid side is given by

$$u_z = 2U \left[1 - \left(\frac{r}{R} \right)^2 \right] \tag{5}$$

where U is the average liquid velocity (m/s) and R the inner radius of the hollow fiber.

3.1. Nitrites in the liquid phase

The inlet concentration for nitrite in the hollow fiber reactor is specified as

At $z = 0$ and all r, $\quad C_l = C_{l,in}$ (6)

where $C_{l,in}$ is the inlet concentration (mol/m^3). At the center of the reactor, symmetry is assumed in radial direction, resulting in the following boundary condition:

At $r = 0$ and all z, $\quad \dfrac{\partial C_l}{\partial r} = 0$ (7)

The additional mass transfer resistance offered by the liquid present in the catalyst layer is also considered. The mass transport is mainly governed by diffusion through the liquid-filled pores matching the consumption by the reaction:

$$D_{l,M} \left(\frac{\partial^2 C_{l,M}}{\partial r^2} + \frac{1}{r} \frac{\partial C_{l,M}}{\partial r} \right) = -R_s \quad (R < r < R+\delta) \tag{8}$$

where $D_{l,M}$ is the diffusion coefficient of nitrite in the catalytic layer (m^2/s), $C_{l,M}$ is the concentration of nitrite in the catalytic layer (mol/m^3), R is the inner channel radius (m), R_s is the reaction rate expression, and δ is the catalytic membrane layer thickness (m). Eq. (8) is based on the assumption that there is no convection in the porous membrane structure and transport through the catalytic membrane layer is driven by diffusion, quantified by the effective diffusion constant $D_{l,M}$ ($= D_l \epsilon / \tau$, where ϵ is the porosity and τ is the tortuosity of the membrane). Since the chemical reaction term (R_s) is a function of concentration, the partial differential equations are not independent and must be solved simultaneously. Assuming that the nitrite concentration used in the experimental work is low, we have considered the power-law reaction rate expression according to Eq. (3) in deriving the boundary conditions. The exponents n and m in Eq. (3) depend on the catalyst surface coverage of nitrite and hydrogen, respectively. The observed reaction rate is limited by the initial reactant concentration and thus, the values for exponents n and m considered to be 1 in deriving the boundary conditions:

At $r = R$ and all z, $\quad D_l \dfrac{\partial C_{l,R}}{\partial r} = D_{l,M} \dfrac{\partial C_{l,M}}{\partial r}$ (9)

where $C_{l,R}$ is the concentration of liquid at position R (mol/m^3). Furthermore,

At $r = R$ and all z, $\quad C_{l,M} = C_{l,R}$ (10)

At $r = R+\delta$ and all z, $\quad \dfrac{\partial C_{l,M}}{\partial r} = 0$ (11)

Use of Eqs. (8)–(11) gives the following boundary condition which includes the mass transport and reaction in the wetted catalytic membrane layer:

At $r = R$ and all z,

$$\frac{\partial C_{l,R}}{\partial r} = \frac{2D_{l,M}}{D_l} \left[\frac{C_{l,R} - C_{l,R+\delta}}{k_1 C_{g,R} (C_{l,R}^2 - C_{l,R+\delta}^2)} \cdot \frac{1}{R[\ln(R+\delta) - \ln R]} \right] \tag{12}$$

where $C_{g,R}$ is the concentration of gas at position R (mol/m^3).

3.2. Hydrogen in the liquid phase

The mass balance for hydrogen in the liquid phase within the microreactor leads to the following boundary conditions:

At $z = 0$ and all r, $\quad C_g = 0$ (13)

where C_g is the concentration of gas (mol/m^3). At the center of the reactor, symmetry is assumed in radial direction, resulting in the following boundary condition:

At $r = 0$ and all z, $\quad \dfrac{\partial C_g}{\partial r} = 0$ (14)

At $r = R+\delta$ and all z, $\quad C_{g,M} = HC_g$ (15)

where H is Henry's coefficient. The mass transport through the liquid phase in the membrane porous structure can be written as

$$D_{g,M} \left(\frac{\partial^2 C_{g,M}}{\partial r^2} + \frac{1}{r} \frac{\partial C_{g,M}}{\partial r} \right) = -R_s \tag{16}$$

where $C_{g,M}$ is the concentration of hydrogen in the catalytic layer (mol/m^3) and $D_{g,M}$ is the diffusion coefficient of hydrogen in the

membrane (m^2/s). At the inner surface

At $r = R$ and all z, $D_g \dfrac{\partial C_{g,R}}{\partial r} = D_{g,M} \dfrac{\partial C_{g,M}}{\partial r}$ (17)

And $r = R$ and all z, $C_{g,M} = C_{g,R}$ (18)

Using Eqs. (15)–(18)

At $r = R$ and all z,

$$\frac{\partial C_{g,R}}{\partial r} = \frac{2D_{g,M}}{D_g}\left[\frac{HC_{g,R+\delta} - C_{g,R}}{k_1 C_{l,R}(C_{g,R+\delta}^2 - C_{g,R}^2)} \cdot \frac{1}{R[\ln(R+\delta) - \ln R]} \right]$$ (19)

3.3. Overall mass transport

The mixing cup concentration ($C_{l,cup}$ (mol/m^3)) can be calculated from the nitrite concentration and velocity product at the reactor outlet:

$$C_{l,cup}(z) = \frac{\int C_l(r) \cdot u_z(r)\, dr}{\int u_z(r)\, dr}$$ (20)

The mixing cup concentration corrects for the velocity with which fluids are flowing and provides the concentration at a respective point considering complete mixing.

The rate of mass transfer to reaction boundaries is represented by the local Sherwood number $Sh(z)$. It can be used as an indicator for the efficiency of a reactant adsorbing on a catalytically active surface [38]. It is defined as

$$Sh(z) = -\frac{N(z)R}{[C_l(z) - C_{l,s}(z)|_{r=R}]D_l}$$ (21)

where $N(z)$ (mol/m^2 s) is the local flux to the surface, $C_l(z)$ (mol/m^3) is the bulk concentration of the liquid reactant calculated according to Eq. (20), and $C_{l,s}(z)$ (mol/m^3) is the liquid reactant concentration at the inner surface of the microreactor (at $r = R$).

Eq. (20) is applied at the microreactor outlet for the validation of numerical results with experimental results, while the local Sherwood number is evaluated along the length of the microreactor.

To provide insight into the performance of the microreactor, the cumulative fraction of adsorbed reactant as a function of the axial position is calculated. The fraction is the ratio of the integrated flux towards the reactive boundaries to the integrated inlet flux. It is an important measure from the design perspective as it suggests effectiveness of the reactor configuration. The local Sherwood number in the limit of small z can provide the fraction of adsorbed reactant on reactive boundaries via [49]

$$f = \frac{Sh(z)}{Pe}\frac{z}{R}$$ (22)

where Pe is the Péclet number ($Pe = UR/D_l$).

3.4. Numerical procedure

The numerical model was solved using COMSOL Multiphysics, which is a finite element modeling tool that facilitates implementation of all governing equations with appropriate boundary conditions. These governing mass balance equations were reduced to their finite element meshes and integrated over the computational domain of interest. The total number of standard triangular mesh elements is 36,409 and the mesh density was increased near the catalytic membrane layer. The mesh is refined until the results become independent of mesh size.

4. Results and discussion

Numerical simulations of the catalytic nitrite hydrogenation reaction in a porous membrane microreactor were performed. Different process parameters (Table 1) such as reactor design parameters (i.e. fiber diameter, catalytic membrane layer thickness,

Table 1
Model parameters and specifications of the porous membrane microreactors.

Porous membrane microreactor	Specifications
Fiber inner radius (mm)	Big fiber—1.4 Small fiber—0.4
Wetted membrane thickness (δ) (μm)	Big fiber—40, 20, 10 Small fiber—50
Reactor length (m)	0.135
Inlet liquid flow rate (mL/min)	0.1, 0.2, 0.3
Initial nitrite concentration (mol/m^3)	0.217, 1.09, 2.17
Diffusion coefficient for nitrite–water (m^2/s)	1.5×10^{-9}
Diffusion coefficient for hydrogen–water (m^2/s)	4.8×10^{-9}
Membrane porosity	0.2
Membrane tortuosity	4
Catalyst area (m^2/g)	73

Fig. 3. Overall conversion for varying adsorption coefficient K_{ads} using the Langmuir–Hinshelwood reaction rate expression. For 40 μm membrane thickness and all inlet nitrite concentrations.
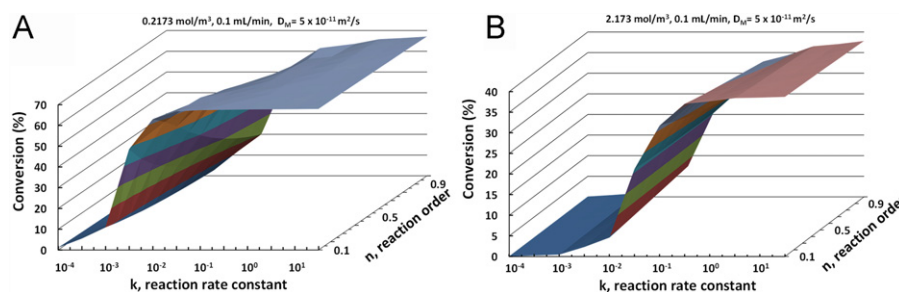

Fig. 2. Parametric study to evaluate the reaction rate constant and reaction order for power-law rate expression. Flow rate 0.1 mL/min, 40 μm membrane thickness: (A) 0.2173 mol/m^3 and (B) 2.1739 mol/m^3.
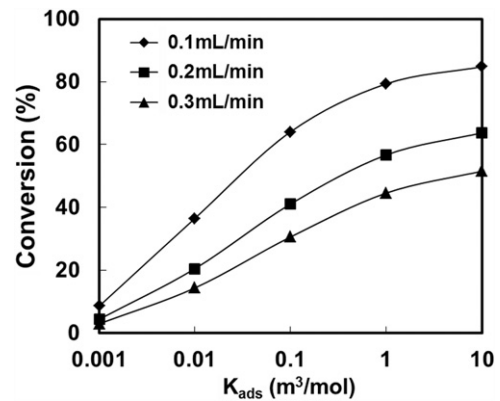
Table 2
Case studied for validation of nitrite hydrogenation reaction rate expression. Comparison of experimental and numerical simulation results for 40 μm catalytic layer thickness. The experimental data are taken from Aran et al. [50].

| Inlet liquid flow rate (mL/min)	Inlet nitrite concentration (mol/m^3)	Experimental conversion (%)	Modeling (LH rate expression)				Modeling (power-law rate expression)			
			Outlet nitrite concentration (mol/m^3)	k_1 (mol/m^3 s)	K_{ads} (m^3/mol)	Conversion (%)	Outlet nitrite concentration (mol/m^3)	n	k_1	Conversion (%)
0.1	0.2173	66.6	0.1434	0.00120	0.1120	66.0	0.1415	0.7	0.175	65.1
0.1	1.0869	36.8	0.4130	0.00125	0.1070	38.0	0.4260	0.5	0.230	39.2
0.1	2.1739	25.3	0.5434	0.00116	0.0075	25.0	0.6130	0.3	0.340	28.2
0.2	0.2173	42.8	0.0934	0.00131	0.1150	43.0	0.0986	0.7	0.175	45.4
0.2	1.0869	21.8	0.2282	0.00135	0.1090	21.0	0.2663	0.5	0.230	24.5
0.2	2.1739	14.9	0.3152	0.00131	0.0074	14.5	0.3826	0.3	0.340	17.6
0.3	0.2173	31.0	0.0695	0.00135	0.1170	32.0	0.0754	0.7	0.175	34.7
0.3	1.0869	15.0	0.1630	0.00134	0.1095	15.0	0.2000	0.5	0.230	18.4
0.3	2.1739	10.3	0.2173	0.00135	0.0075	10.0	0.3021	0.3	0.340	13.9
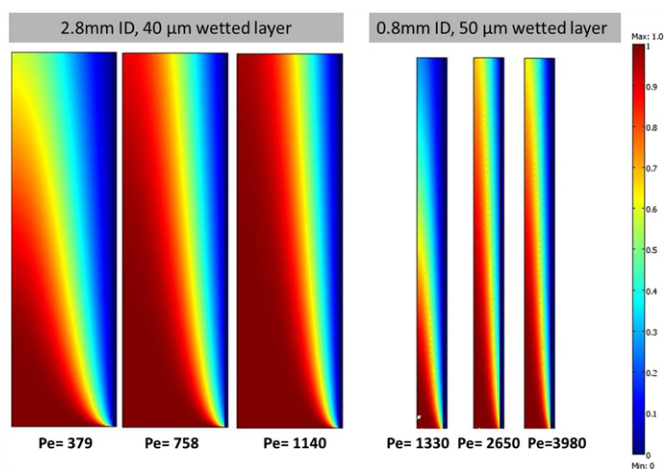
Fig. 4. Concentration profiles for a larger fiber (2.8 mm ID) and small fiber (0.8 mm ID) for different flow rates. In order to evaluate the model, a transverse Péclet number ($Pe_{trans} = UR^2/D_lL$) number has been put into perspective.

porosity, tortuosity, reactor length) and operational parameters (i.e., reactant concentrations, liquid flow rates) were studied.

4.1. Obtaining the reaction rate expression

To validate the proposed model, the nitrite hydrogenation reaction was taken as a model reaction. The operating conditions and reactor geometry used are similar to experimental conditions used by Aran et al. [29,50]. The values of the reaction constant and reaction order according to Eq. (3) are varied and the resulting overall conversion is shown in Fig. 2. It is assumed that the reaction rate is not dependent on hydrogen concentration as was also confirmed by recent experiments [29]. Fig. 3 shows the conversion obtained considering the LH rate expression according to Eq. (2). The results obtained from the reaction rate expression study (power-law and Langmuir–Hinshelwood reaction rate) are shown in Table 2 for varying inlet nitrite concentration and liquid flow rates. For the power-law reaction rate expression, the numerical results are in good agreement with the experimental results at lower initial nitrite concentration for all flow rates. However, it is found that the kinetic expression represented in Eq. (3) is not in good agreement with experimental results at higher initial nitrite concentration. A possible explanation for this can be a zeroth-order reaction at higher nitrite concentration resulting from saturated conditions. This phenomenon is captured by the Langmuir–Hinshelwood expression described in Eq. (2).
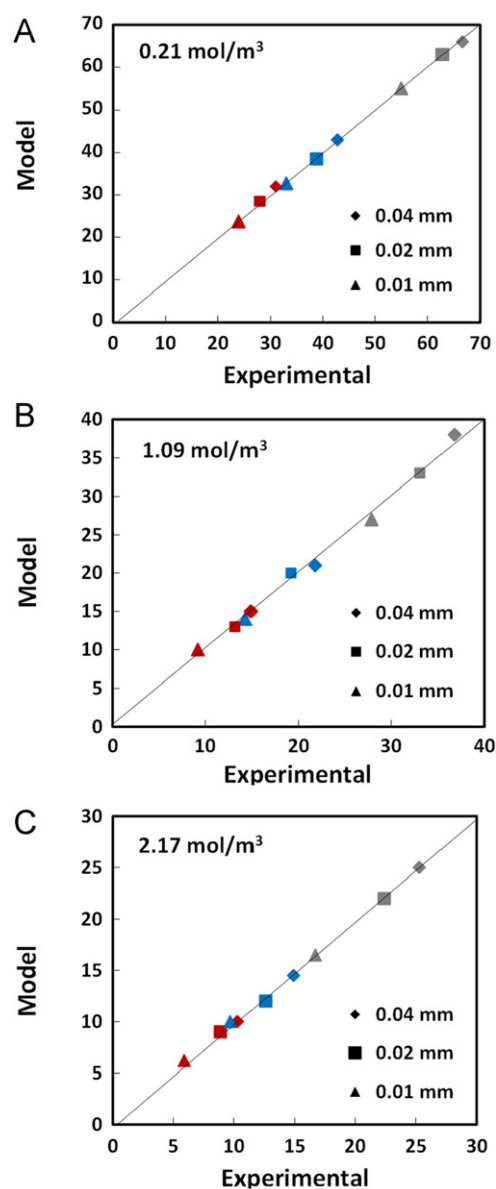

Fig. 5. Parity plot of the nitrite hydrogenation conversion for three different concentrations for 2.8 mm ID reactor. Study of three catalytic wetting layer thickness (40, 20 and 10 μm) and three different Pe_{trans} = 3.93 (in red), 7.86 (in blue) and 11.82 (in gray): (A) 0.21 mol/m^3, (B) 1.09 mol/m^3, and (C) 2.17 mol/m^3. (For interpretation of the references to color in this figure caption, the reader is referred to the web version of this article.)

The parameters k_{LH} and K_{ads} in Eq. (2) have been determined by fitting the model to the experimental data obtained from Aran et al. [50]. The value of k_{LH} is found to be 0.0013 mol/m^3 s (95% of confidence interval within $\pm$ 0.00005) and K_{ads} to be 0.08 m^3/mol (95% of confidence interval within $\pm$ 0.04) for all the process conditions. A good agreement between the experimental results and model predictions based on the Langmuir–Hinshelwood reaction rate expression (Fig. 3 and Table 2) is found.

4.2. Nitrite hydrogenation in membrane microreactors

Fig. 4 shows typical concentration profiles for different Péclet numbers for two microreactor diameters. As can be seen, a boundary layer appears near the wall of the reactor which grows in thickness with increasing distance along the reactor length. This results from the depletion of reactants from the region adjacent to the reaction zone (near the γ-Al$_2$O$_3$ layer).

The internal diameter of the microreactor, the catalytic membrane layer thickness and the inlet liquid flow rate play a major role in the mass transfer, which strongly affects the overall conversion. The total nitrite removal in different microreactor configurations is calculated at the microreactor outlet by measuring the mixing cup concentration equation (20). In order to validate the values of LH kinetic parameters, parity plots are presented comparing numerical results with experimental observations in Fig. 5, for varying inlet nitrite concentration, wetting thickness and $Pe_{trans}(=UR^2/D_lL)$ numbers. Using the LH reaction rate expression, the numerical results show good agreement with the experimental results for a wide range of conditions.

The liquid reactant concentration profile can be obtained at the inner wall of the microreactor along the axial direction of the microreactor length. Eqs. (3)–(19) are coupled and solved simultaneously using a general-partial differential equation solver (in COMSOL). In Fig. 6, the concentration profile along the microreactor wall using this approach is plotted together with the concentration profile obtained from 2D CFD model (which solves (2) and (4)–(11) without taking into account the hydrogen transport in the catalytic layer). The results are in good agreement, suggesting the applicability of the model. This explains that with the proposed boundary conditions, represented by Eqs. (12) and (1), it is possi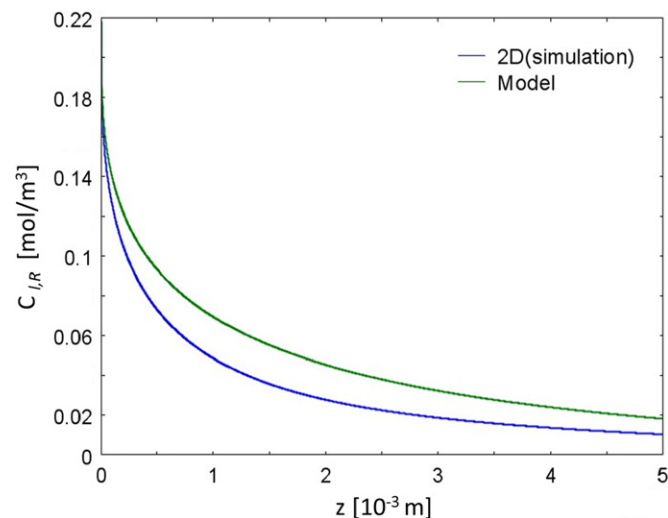ble to obtain an expression representing the concentration of reactants as a function of catalytic membrane layer thickness.

Fig. 7 shows the influence of the catalytic membrane layer thickness on the reactor performance. The average nitrite concentration at the microreactor wall initially decreases with increasing membrane thickness. This is due to the larger amount of available catalyst surface area. Further increasing the catalytic layer thickness will eventually result in mass transport limitations from the gas side.
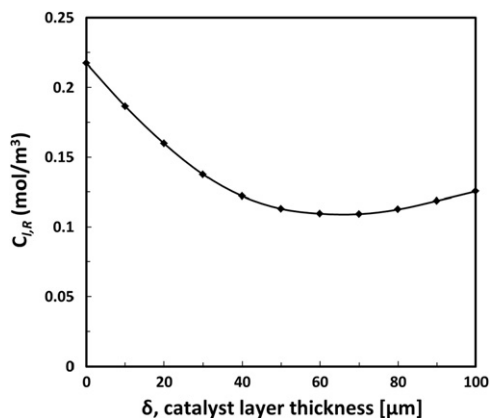

Fig. 7. Influence of catalytic membrane layer thickness on the average reactant concentration at the microreactor wall for 0.2173 mol/m^3 initial nitrite concentration and 0.1 mL/min flow rate (L=0.135 m, D_l=1 × 10^{-9} m^2/s, D_g=4.8 × 10^{-9} m^2/s, ϵ = 0.2, τ = 4.0).

Fig. 6. Reactant concentration profile at the microreactor wall as a function of the axial position for 40 μm catalytic membrane layer thickness, 0.2173 mol/m^3 initial nitrite concentration and 0.1 mL/min flow rate (L=0.135 m, D_l=1 × 10^{-9} m^2/s, D_g=4.8 × 10^{-9} m^2/s, ϵ = 0.2, τ = 4.0) (For interpretation of the references to color in this figure caption, the reader is referred to the web version of this article.).
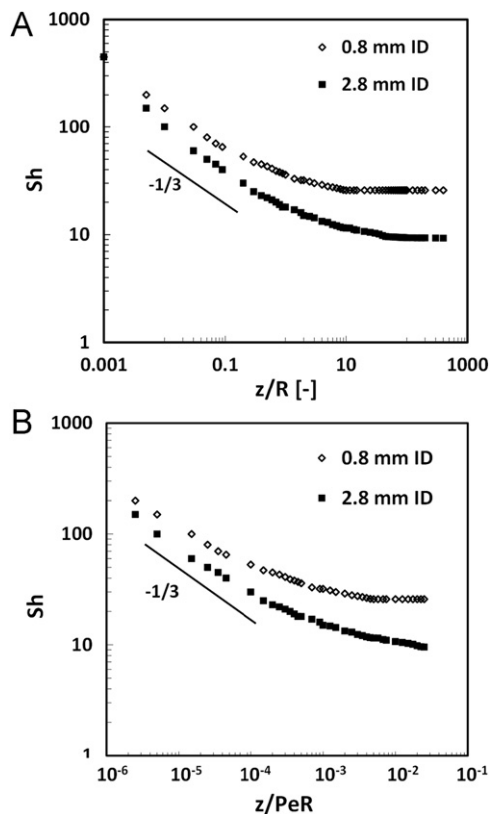
Fig. 8. (A) Comparison of the local Sherwood number to an adsorbing reaction boundary along the axial position of the microreactor for 2.8 mm and 0.8 mm ID reactor geometry for Pe_{trans}=20.74. (B) Sherwood number as a function of axial distance scaled by Pe.
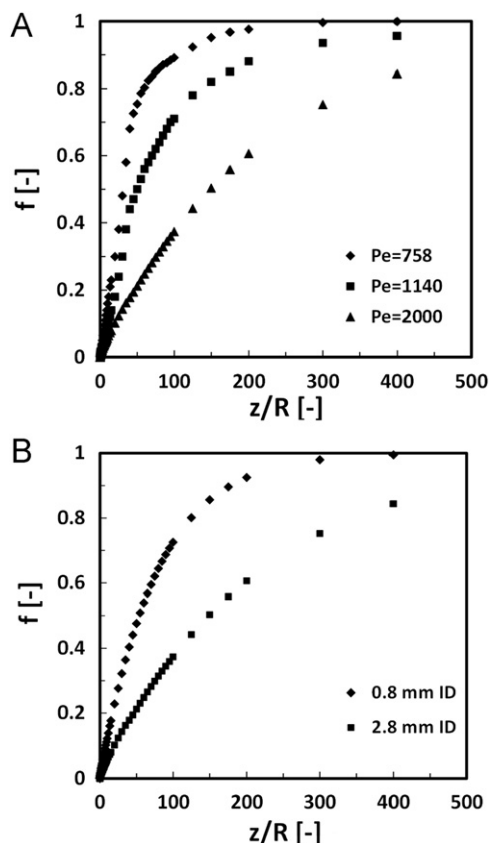
Fig. 9. A fraction of adsorbed reactant concentration plotted as a function of the axial position. (A) For the big fiber (2.8 mm ID) for Pe_{trans} 7.86, 11.82 and 20.74. (B) For both reactor configurations for $Pe_{trans}=20.74$.

Sherwood numbers are plotted against the dimensionless axial position (z/R) according to Eq. (21) in Fig. 8A ($Pe=2000$). For very small axial distances, the depletion layer is just starting to form. The depletion layer significantly grows at larger axial positions for the larger reactor configuration compared to the smaller reactor. For the small ID reactors, the boundary layer thickness is relatively small, which improves transport even at large axial positions. These observations also agree qualitatively with previous work [38,49]. The operating conditions used in previous studies were different, so results cannot be compared quantitatively. However, the simulations of both geometries, (for $Pe_{trans}=20.74$) confirm the theoretical values of $-1/3$ for the power law scaling of the Sherwood number (assuming a smooth inside microreactor surface) near the reactor entrance region.

Furthermore, Fig. 8B shows that $Sh(z)$ scales with $(z/PeR)^{-1/3}$. The larger fibers (2.8 mm ID) results in an entrance length of $(z_{ent}/PeR) \sim 1 \times 10^{-2}$. In case of the smaller fiber (0.8 mm ID), the concentration distribution is approaching its asymptotic value at shorter scaled axial distances ($z_{ent}/PeR \sim 3 \times 10^{-3}$), which suggests better performance compared to the bigger fibers. The smaller fiber provides a higher rate of mass transport by sweeping the depleted solute off near the catalytic layer. It leads to thinner boundary layers compared to the bigger fiber (2.8 mm ID).

The fraction of adsorbed liquid reactant (nitrite) is calculated (Eq. (22)) for different operating conditions and reactor configurations. The fraction f approaches unity for an ideal reactor, where all liquid reactants entering into the reactor are adsorbed and reacted. Fig. 9A shows f plotted against the axial position for large fibers (2.8 mm ID) and different values of Pe_{trans} (7.86, 11.82 and 20.74). For each Pe_{trans}, the fraction f increases along the

reactor length. It can be observed that a smaller Pe_{trans} (and hence a larger residence time) results in a significant increase in this fraction. From these plots, the desired reactor length can be easily extracted.

Fig. 9B shows a comparison between the two diameters for the case of $Pe_{trans}=20.74$. For the small diameter reactor, the fraction f increases steeper compared to the large diameter. It reaches unity at around $z/R \approx 300$, while the fraction for ID 2.8 mm fiber is approximately 0.7 at that distance. For the same value of Pe number (in the range of 100–400z/R), the smaller fiber increases this fraction from 70% to 100% compared to fraction for the larger diameter which increases from 30% to 80%. It is apparent from the plot that the smaller diameter reactor is more effective in reducing the depletion layer near the reactive boundary.

5. Conclusions

We present a model for a porous membrane microreactor to simulate a wide range of operating conditions and microreactor configurations. The analysis includes a description of the reaction mechanism verified by experimental observations. The proposed model and numerical simulations were validated with experimental data obtained from reactor experiments at varying initial reactant concentrations, inlet flow rates and microreactor geometries. It was found that nitrite hydrogenation in a porous membrane microreactor can be described by the Langmuir–Hinshelwood expression. An accurate description of the boundary condition representing the concentration as a function of catalytic membrane layer thickness has been successfully derived. By comparing several flow rates and reactor diameters, it is concluded that small reactor geometries are important to achieve increased mass transfer to reactive boundaries. The numerical model provides a tool that can be used for the design of such membrane microreactors.

References

[1] V. Hessel, P. Angeli, A. Gavriilidis, H. Löwe, Gas–liquid and gas–liquid–solid microstructured reactors: contacting principles and applications, Ind. Eng. Chem. Res. 44 (25) (2005) 9750–9769.
[2] P. Mills, D. Quiram, J. Ryley, Microreactor technology and process miniaturization for catalytic reactions—a perspective on recent developments and emerging technologies, Chem. Eng. Sci. 62 (24) (2007) 6992–7010.
[3] J. de Jong, M. Geerken, R. Lammertink, M. Wessling, Porous microfluidic devices—fabrication and applications, Chem. Eng. Technol. 30 (3) (2007) 309–315.
[4] G. Centi, R. Dittmeyer, S. Perathoner, M. Reif, Tubular inorganic catalytic membrane reactors: advantages and performance in multiphase hydrogenation reactions, Catal. Today 79 (2003) 139–149.
[5] M. Harold, C. Lee, Intermediate product yield enhancement with a catalytic inorganic membrane—II. Nonisothermal and integral operation in a back-mixed reactor, Chem. Eng. Sci. 52 (12) (1997) 1923–1939.
[6] J. Coronas, J. Santamaria, Catalytic reactors based on porous ceramic membranes, Catal. Today 51 (3–4) (1999) 377–389.
[7] T. Tsotsis, A. Champagnie, S. Vasileiadis, Z. Ziaka, R. Minet, Packed bed catalytic membrane reactors, Chem. Eng. Sci. 47 (9–11) (1992) 2903–2908.
[8] H. Sloot, G. Versteeg, W. Van Swaaij, A non-permselective membrane reactor for chemical processes normally requiring strict stoichiometric feed rates of reactants, Chem. Eng. Sci. 45 (8) (1990) 2415–2421.
[9] R. Dittmeyer, K. Svajda, M. Reif, A review of catalytic membrane layers for gas/liquid reactions, Top. Catal. 29 (1) (2004) 3–27.
[10] G. Chen, J. Yue, Q. Yuan, Gas–liquid microreaction technology: recent developments and future challenges, Chin. J. Chem. Eng. 16 (5) (2008) 663–669.

[11] T. Westermann, T. Melin, Flow-through catalytic membrane reactors—principles and applications, Chem. Eng. Process: Process Intensification 48 (1) (2009) 17–28.

[12] H. Fogler (Ed.), Elements of Chemical Reaction Engineering, 3rd ed.,Prentice Hall and Englewood Cliffs, New Jersey, 1999.

[13] A. Beenackers, W. Van Swaaij, Mass transfer in gas–liquid slurry reactors, Chem. Eng. Sci. 48 (18) (1993) 3109–3139.

[14] E. Dietrich, C. Mathieu, H. Delmas, J. Jenck, Raney-nickel catalyzed hydrogenations: gas–liquid mass transfer in gas-induced stirred slurry reactors, Chem. Eng. Sci. 47 (13) (1992) 3597–3604.

[15] E. Alper, B. Wichtendahl, W. Deckwer, Gas absorption mechanism in catalytic slurry reactors, Chem. Eng. Sci. 35 (1–2) (1980) 217–222.

[16] W. Bruining, G. Joosten, A. Beenackers, H. Hofman, Enhancement of gas–liquid mass transfer by a dispersed second liquid phase, Chem. Eng. Sci. 41 (7) (1986) 1873–1877.

[17] V. Hessel, P. Angeli, A. Gavriilidis, H. Löwe, Gas–liquid and gas–liquid–solid microstructured reactors: contacting principles and applications, Ind. Eng. Chem. Res. 44 (25) (2005) 9750–9769.

[18] A. Colombo, G. Baldi, S. Sicardi, Solid–liquid contacting effectiveness in trickle bed reactors, Chem. Eng. Sci. 31 (12) (1976) 1101–1108.

[19] P. Mills, M. Dudukovic, Evaluation of liquid–solid contacting in trickle-bed reactors by tracer methods, AIChE J. 27 (6) (1981) 893–904.

[20] A. Gianetto, G. Baldi, V. Specchia, S. Sicardi, Hydrodynamics and solid–liquid contacting effectiveness in trickle-bed reactors, AIChE J. 24 (6) (1978) 1087–1104.

[21] A. Attou, C. Boyer, G. Ferschneider, Modelling of the hydrodynamics of the cocurrent gas–liquid trickle flow through a trickle-bed reactor, Chem. Eng. Sci. 54 (6) (1999) 785–802.

[22] I. Iliuta, F. Larachi, B. Grandjean, G. Wild, et al., Gas–liquid interfacial mass transfer in trickle-bed reactors: state-of-the-art correlations, Chem. Eng. Sci. 54 (23) (1999) 5633–5645.

[23] M. Losey, M. Schmidt, K. Jensen, Microfabricated multiphase packed-bed reactors: characterization of mass transfer and reactions, Ind. Eng. Chem. Res. 40 (12) (2001) 2555–2562.

[24] M. Vospernik, A. Pintar, G. Bercic, J. Batista, J. Levec, Potentials of ceramic membranes as catalytic three-phase reactors, Chem. Eng. Res. Des. 82 (5) (2004) 659–666.

[25] A. Pintar, G. Bercic, J. Levec, Catalytic liquid-phase nitrite reduction: kinetics and catalyst deactivation, AIChE J. 44 (10) (1998) 2280–2292.

[26] J. Chinthaginjala, L. Lefferts, Support effect on selectivity of nitrite reduction in water, Appl. Catal. B: Environ. 101 (1–2) (2010) 144–149.

[27] O. Ilinitch, F. Cuperus, L. Nosova, E. Gribov, Catalytic membrane in reduction of aqueous nitrates: operational principles and catalytic performance, Catal. Today 56 (1–3) (2000) 137–145.

[28] M. Vospernik, A. Pintar, G. Bercic, J. Levec, Experimental verification of ceramic membrane potentials for supporting three-phase catalytic reactions, J. Membr. Sci. 223 (1–2) (2003) 157–169.

[29] H. Aran, J. Chinthaginjala, R. Groote, R. Roelofs, L. Lefferts, M. Wessling, R. Lammertink, Porous ceramic mesoreactors: a new approach for gas–liquid contacting in multiphase microreaction technology, Chem. Eng. J. 169 (1–3) (2011) 239–246.

[30] G. Bercic, A. Pintar, J. Levec, Positioning of the reaction zone for gas–liquid reactions in catalytic membrane reactor by coupling results of mass transport and chemical reaction study, Catal. Today 105 (3–4) (2005) 589–597.

[31] P. Cini, M. Harold, Experimental study of the tubular multiphase catalyst, AIChE J. 37 (7) (1991) 997–1008.

[32] R. Wang, H. Zhang, P. Feron, D. Liang, Influence of membrane wetting on CO2 capture in microporous hollow fiber membrane contactors, Sep. Purif. Technol. 46 (1–2) (2005) 33–40.

[33] S. Kumar, S. Shankar, P. Shah, S. Kumar, A comprehensive model for catalytic membrane reactor, Int. J. Chem. React. Eng. 4 (4) (2006) 1296.

[34] C. Tsai, Y. Ma, R. William, G. Anthony, Modeling and simulation of a nonisothermal catalytic membrane reactor, Chem. Eng. Commun. 134 (1) (1995) 107–132.

[35] E. Nagy, Mass Transfer through a convection flow catalytic membrane layer with dispersed nanometer-sized catalyst, Ind. Eng. Chem. Res. 49 (3) (2009) 1057–1062.

[36] K. Li, X. Tan, Mass transfer and chemical reaction in hollow-fiber membrane reactors, AIChE J. 47 (2) (2001) 427–435.

[37] T. Gervais, K. Jensen, Mass transport and surface reactions in microfluidic systems, Chem. Eng. Sci. 61 (4) (2006) 1102–1121.

[38] J. Kirtland, G. McGraw, A. Stroock, Mass transfer to reactive boundaries from steady three-dimensional flows in microchannels, Phys. Fluids 18 (2006) 073602.

[39] S. Oyama, P. Hacarlioglu, The boundary between simple and complex descriptions of membrane reactors: the transition between 1-D and 2-D analysis, J. Membr. Sci. 337 (1–2) (2009) 188–199.

[40] W. Moon, S. Park, Design guide of a membrane for a membrane reactor in terms of permeability and selectivity, J. Membr. Sci. 170 (1) (2000) 43–51.

[41] W. Jin, X. Gu, S. Li, P. Huang, N. Xu, J. Shi, Experimental and simulation study on a catalyst packed tubular dense membrane reactor for partial oxidation of methane to syngas, Chem. Eng. Sci. 55 (14) (2000) 2617–2625.

[42] W. Yu, T. Ohmori, T. Yamamoto, A. Endo, M. Nakaiwa, T. Hayakawa, N. Itoh, Simulation of a porous ceramic membrane reactor for hydrogen production, Int. J. Hydrogen Energy 30 (10) (2005) 1071–1079.

[43] C. Fukuhara, A. Igarashi, Two-dimensional simulation of a membrane reactor for dehydrogenation of ethylbenzene, considering heat and mass transfer, J. Chem. Eng. Jpn. 36 (5) (2003) 530–539.

[44] T. Brinkmann, S. Perera, W. Thomas, An experimental and theoretical investigation of a catalytic membrane reactor for the oxidative dehydrogenation of methanol, Chem. Eng. Sci. 56 (6) (2001) 2047–2061.

[45] K. Hoff, J. Poplsteinova, H. Jakobsen, O. Falk-Pedersen, O. Juliussen, H. Svendsen, Modeling of membrane reactor, Int. J. Chem. React. Eng. 1 (1) (2002) 1011.

[46] N. Wehbe, N. Guilhaume, K. Fiaty, S. Miachon, J. Dalmon, Hydrogenation of nitrates in water using mesoporous membranes operated in a flow-through catalytic contactor, Catal. Today 156 (3–4) (2010) 208–215.

[47] M. Reif, R. Dittmeyer, Porous, catalytically active ceramic membranes for gas–liquid reactions: a comparison between catalytic diffuser and forced through flow concept, Catal. Today 82 (1–4) (2003) 3–14.

[48] U. Matatov-Meytal, Radial-flow reactor packed with a catalytic cloth: nitrate reduction in hydrogen-saturated water, Ind. Eng. Chem. Res. 44 (25) (2005) 9575–9580.

[49] M. Lopez, M. Graham, Enhancement of mixing and adsorption in microfluidic devices by shear-induced diffusion and topography-induced secondary flow, Phys. Fluids 20 (2008) 053304.

[50] H. Aran, Porous Ceramic and Metallic Microreactors: Tuning Interfaces for Multiphase Processes, Ph.D. Thesis, 2011.